JGR Oceans

RESEARCH ARTICLE

10.1029/2019JC015898

Estimating Southern Ocean Storm Positions With Seismic Observations

Momme C. Hell[1], **Sarah T. Gille**[1], **Bruce D. Cornuelle**[1], **Arthur J. Miller**[1], **Peter D. Bromirski**[1], **and Alex D. Crawford**[2,3]

[1]Scripps Institution of Oceanography, University of California, San Diego, La Jolla, CA, USA, [2]National Snow and Ice Data Center, Cooperative Institute for Research in Environmental Sciences, University of Colorado Boulder, Boulder, CO, USA, [3]Department of Earth Sciences, The College of Wooster, Wooster, OH, USA

Key Points:

- Ocean swell events are detected in the Ross Ice shelf year-round, but 45% or less of the swell can be linked with individual storms
- About 55% or more of the observed swell can only be associated with reanalysis winds whose positions are displaced
- Reanalysis winds are often displaced when sparse or no observations of surface winds are available, as for example, over or close to sea ice

Supporting Information:

- Supporting Information S1

Correspondence to:
M. Hell,
mhell@ucsd.edu

Citation:
Hell, M. C., Gille, S. T., Cornuelle, B., Miller, A. J., Bromirski, P. D., & Crawford, A. D. (2020). Estimating Southern Ocean storm positions with seismic observations. *Journal of Geophysical Research: Oceans*, *125*, e2019JC015898. https://doi.org/10.1029/2019JC015898

Received 27 NOV 2019
Accepted 14 MAR 2020
Accepted article online 1 APR 2020

Abstract Surface winds from Southern Ocean cyclones generate large waves that travel over long distances (>1,000 km). Wave generation regions are often colocated with enhanced air-sea fluxes and upper ocean mixing. Ocean wave spectra contain information about storm wind speed, fetch size, and intensity at their generation site. Two years of seismic observations on the Ross Ice shelf, combined with modern optimization (machine learning) techniques, are used to trace the origins of wave events in the Southern Ocean with an accuracy of ±110 km and ±2 hr from a hypothetical point source. The observed spectral energy attenuated within sea ice and in the ice shelf but retains characteristics that can be compared to parametric wave models. Comparison with the Modern-Era Retrospective Analysis for Research and Applications, Version 2, and ERA5 reanalyses suggests that less than 45% of ocean swell events can be associated with individual Southern Ocean storms, while the majority of the observed wave events cannot be matched with Southern Ocean high wind events. Reanalysis cyclones and winds are often displaced by about 350 km or 10 hr in Modern-Era Retrospective Analysis for Research and Applications, Version 2, and ERA5 compared to the most likely positions inferred from the seismic spectra. This high fraction of displaced storms in reanalysis products over the South Pacific can be explained by the limited availability of remote sensing observations, primarily caused by the presence of sea ice. Deviation of wave rays from their great circle path by wave-current interaction plays a minor role.

Plain Language Summary Surface winds under storms over the Southern Ocean make large ocean waves that travel over long distances (>1,000 km). Regions of wave generation coincide with regions where ocean uptake of heat and CO_2 is large, so knowledge about wave generation regions helps us to understand the role of the Southern Ocean in the climate system. A 2-year field campaign made new observations of ocean wave arrivals at the Ross Ice Shelf. These observations are used to trace the origins of the wave events in the Southern Ocean. Even though the waves observed in the sea ice are much smaller than in the open ocean, the observations are good enough to identify ocean waves. The wave arrivals can be used to infer a most likely time and location of the storm that generated the waves. Comparison with two reanalysis products (Modern-Era Retrospective Analysis for Research and Applications, Version 2, and ERA5) suggests that more than half of the observed ocean wave events cannot be matched to individual Southern Ocean storms. This high percentage of displaced storms in the reanalysis products can be explained by the limited availability of satellite observations caused by the presence of sea ice.

1. Introduction

Southern Hemisphere extratropical cyclones are among the strongest cyclones on the planet, with surface wind speeds that can exceed 35 m s^{-1}. They establish a region of variable and high wind speeds in the Southern Ocean storm track (Hoskins & Hodges, 2005; Simmonds et al., 2003; Trenberth, 1991). These high winds are associated with the generation of wave events and the regulation of heat and momentum surface fluxes, as well as biological production in the ocean mixed layer (Arrigo et al., 2015; Bourassa et al., 2013; Carranza et al., 2018; Gruber et al., 2019; Miles, 1960; Smith, 1988). By driving these fluxes, surface winds play an important role in the coupled climate system. In the Southern Ocean, at least three mechanisms govern the response of the ocean, atmosphere, and cryosphere to wind variability.

First, surface winds drive the ocean circulation via direct surface drag, by regulating freshwater fluxes via sea ice advection (Abernathey et al., 2016), or by maintaining large atmosphere-ocean temperature gradients at the Antarctic continent (Abernathey et al., 2016; Comiso et al., 2011; Haumann et al., 2016; Holland & Kwok, 2012; Johnson & Bryden, 1989; Kwok, 2005; Munk & Palmén, 1951). In many of these processes, surface winds are assumed to exert a zonal mean force. However, within the storm track, winds are spatially heterogeneous because they are located behind atmospheric fronts, resulting in the forcing being not consistently zonal (Beare, 2007; Neiman & Shapiro, 1993; Neiman et al., 1993).

Second, the upper ocean influences the development of cyclones by moderating the availability of heat and moisture. It regulates production of low-level potential vorticity and consequently the cyclone life cycle. Evidence suggests that regions of storm generation and decay, as well as storm intensification, are influenced by SST gradients, sea ice, and topography (e.g., Ceppi et al., 2017; Hoskins & Hodges, 2005; Kidston et al., 2011; Lu et al., 2010; Simmonds & Murray, 1999).

Third, precipitation on sea ice and the Antarctic continent is driven by cyclone dynamics. A good estimate of snowfall on the Antarctic continent is needed to understand ice sheet mass balances in order to anticipate their future contribution to sea level rise (Shepherd et al., 2012). In summary, understanding the variability and defining parameters of Southern Ocean cyclones is important for understanding the coupled variability of the Southern Ocean on all time scales, and the associated impacts on Antarctic processes.

The severe weather and difficult access to the region around Antarctica limit in situ observations, making remote sensing techniques essential for observing surface processes. Satellite observations produce spatially well-resolved snapshots of surface winds that allow a detailed view of surface processes. However, the sparseness of in situ observations in the Southern Ocean impedes the calibration of remote sensing estimates. In particular, a lack of observations of extratropical cyclones and severe weather conditions can cause biases to be largest where the winds are strongest (Ardhuin et al., 2010; Chawla et al., 2013; Rascle et al., 2008). These biases correspond to biases in wave climate and surface momentum fluxes (Bourassa et al., 2013; Bidlot et al., 2002; Cavaleri, 2009; Li et al., 2013) and upper ocean mixing (Li et al., 2016). The biases may also have an impact on the assessment of the total energy input by wind (Ferrari & Wunsch, 2010; Rascle et al., 2008)

The lack of in situ surface wind sampling can lead to errors in reanalysis products and wave models. For example, the addition of a single mooring at the Ocean Observatories Initiative site in the southeast Pacific had a significant impact on the regional weather forecast produced by the European Centre for Medium-Range Weather Forecasts (Ogle et al., 2018). Anecdotally, this suggests that Southern Hemisphere reanalysis deficiencies in representing synoptic scale variability could stem from lack of observations. An objective of this study is to provide a quantifiable measure of the accuracy of Southern Ocean storm positions determined from reanalysis products, which will allow refinement of our understanding of Southern Ocean surface processes and improvement of Southern Ocean wind products.

This study takes advantage of 2 years of continuous seismic observations (Wiens et al., 2014) collected on the Ross Ice Shelf (RIS), using a wave event identification methodology developed for these data by Hell et al. (2019). The methodology uses spectrograms of swell arrivals to estimate the position and time of Southern Ocean high wind events under cyclones (described in sections 3.1 and 3.2). We show here (i) that this method can be used to validate state-of-the-art reanalysis products (section 4.1) and (ii) that swell from storms travels through the sea ice and impacts the Ross Ice Shelf. The methodology provides a means to verify ocean wave products and to examine both sea ice-wave interactions and the impact of ocean swell on ice shelves (Chen et al., 2019; Massom et al., 2018; Ren & Leslie, 2014).

2. Southern Hemisphere Storm Tracking by Forerunners of Swell—A Case Study

Strong wind patterns over the Southern Ocean are generated by extratropical cyclones. Each storm undergoes a characteristic life cycle of generation (cyclogenesis), intensification, and decay (cyclolysis). This life cycle is connected to the large-scale baroclinicity and to local surface conditions, such as topography or convection (Neiman & Shapiro, 1993; Simmonds & Murray, 1999; Simmonds & Keay, 2000). Figure 1 shows an example of a storm life cycle, in this case for a storm in July/August 2015 (thick black line in Figure 1a).

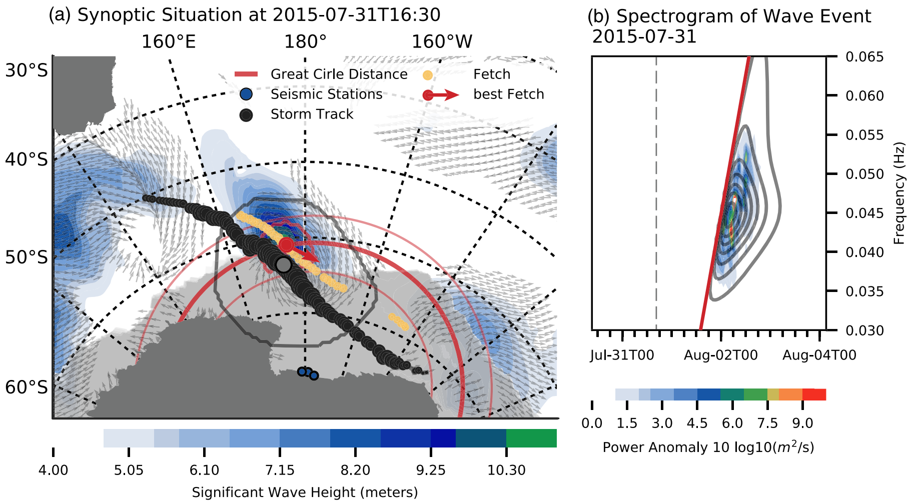

Figure 1. Example of a Southern Ocean storm (a) in reanalysis and (b) the spectrograms response at the ice shelf front to the same storm. (a) Synoptic situation at t_0, the time when waves under the storm start to disperse, with the thick black line as the storm track, the gray dot as its intensity maximum, and the single gray contour as the cyclone area. The orange dots indicate fetch centers associated with the storm track (see section 3.4), and the red dot is the fetch center at t_0, while the fetch area is the red contour. Small gray arrows indicate surface winds (> 10 m s^{-1}), blue shading shows significant wave heights (>4 m, WW3 with ECMWF winds), and the gray area illustrates the sea ice concentration (SIC) using ESA Sea Ice CCI products (Toudal Pedersen et al., 2017). The red semicircles illustrates the estimated radial distance from the seismic stations (dark blue dots) using the slope of the dispersion trend in the seismic observations in (b) and the wave's group velocity (1) with its 95% confidence interval (thin red semicircles). (b) Spectrogram of the corresponding wave event in (a) during July 2015. The shading shows the acceleration spectrum from a seismic station at the central dark blue dot in (a), the gray contours are the fitted model (section 3.2), the red line is the estimated dispersion slope (Hell et al., 2019), and the gray dashed line is the initial time t_0.

Reanalysis studies suggest that the highest winds are often found on the equatorward side of the cyclone center (Figure 1a, orange dots; Bengtsson et al., 2009; Hodges et al., 2011), so that they move at speeds similar to those of the cyclone centers, about 10–35 m s^{-1}.

Strong winds work on the ocean surface and create wind waves, which lead to the generation of swell waves (Figure 1a, shading shows significant wave height; Hasselmann et al., 1985). Swell properties, such as amplitude and frequency, depend on the “fetch,” defined to represent the area over which winds act quasi-stationary, that is with uniform strength and duration (Figure 1a, red outlined area Barnett, 1968; Hasselmann, 1963; Kudryavtsev et al., 2015; Pierson & Moskowitz, 1964). The mechanisms by which winds generate waves in the fetch area are still an active research question. However, third-generation parametric wave models are able to generate realistic wave spectra using 10 m or surface winds (gray arrows in Figure 1a; Chawla et al., 2013; Cavaleri, 2009; Tolman, 2009).

If far-field effects are neglected, wind speed and wind duration control the local wave field (Phillips, 1985). Once waves travel out of their generation region, they disperse, dissipate, and can be interpreted as a group of linear gravity waves propagating across the ocean. Wave event spectra have characteristic peak frequencies and amplitudes that are connected to the wind speeds and fetch in the generation region (Hasselmann, 1963; Pierson & Moskowitz, 1964). However, the fetch over the open ocean is often weakly defined, and these semiempirical models do not consider the wind acting on the ocean in an irregular region that is moving and changing form.

Swell waves generated by storms can travel long distances (Munk & Snodgrass, 1957; Snodgrass et al., 1966), and when they interact with sea ice, higher frequencies are damped, or reflected (Fox & Squire, 1994; Squire, 2007; Vaughan et al., 2009). The remaining low-frequency energy travels through the sea ice and is observed in seismic records from the ice shelves (Figure 1 b, shading; Bromirski et al., 2010; Cathles et al., 2009; Collard et al., 2009; Hell et al., 2019; MacAyeal et al., 2009). These seismic spectrograms show a systematic shift of peak frequency with time (Figure 1b, red line; Barber & Ursell, 1948; Bromirski et al., 2010; Munk, 1947; Snodgrass et al., 1966), which is explained by the deep water dispersion relation of ocean swell

$$\omega^2 = kg, \tag{1}$$

where $\omega = 2\pi f$, with f being the frequency of the wave, k the wave number, and g the acceleration due to gravity. The group velocity is frequency dependent, meaning that longer waves travel faster. The group velocity of the wave group is

$$c_g = \frac{\partial\omega}{\partial k} = \frac{1}{2}\sqrt{\frac{g}{k}} = \frac{gT}{4\pi} = \frac{\Delta x}{\Delta t}, \tag{2}$$

with T as the wave period (Barber & Ursell, 1948; Munk, 1947). For an observed wave with a given frequency, this relates the distance traveled (Δx) and travel time (Δt, Figure 1a, red semicircular arcs). In other words, if one observes a wave of a given frequency and knows how far it has propagated, then the time of origin can be inferred. Or, if one observes two waves of different frequency and assumes they come from the same source, then both the time of origin and the distance traveled can be estimated.

This principle can be used in combination with spectrograms of ocean waves, mostly from wave buoys, to estimate the travel distance and time of wave generation (Barber & Ursell, 1948; Bromirski & Duennebier, 2002; Gallet & Young, 2014; Munk, 1947; Snodgrass et al., 1966). As explained in detail below, the same phenomenon is observed in spectrograms of seismic observations from ice shelves (Figure 1b, Bromirski et al., 2010; Cathles et al., 2009; MacAyeal et al., 2009). Seismic data from the ice shelf can be used to invert spectrogram slope to estimate propagation time and radial distance to the origin (equation (2); Munk, 1947; Munk et al., 1963). Figure 1a shows the synoptic situation at the estimated initial time (gray line in Figure 1b), and the red semicircular arcs provide estimates of the radial distances from the ice shelf seismic station. Both are derived from the red dispersion slope in Figure 1b.

A standard assumption is that each wave event is generated at a point source and travels undisturbed along a great circle path. This is a strong simplification (Figure 1a) but works surprisingly well (Collard et al., 2009; Snodgrass et al., 1966). In reality, swell waves are generated by fast moving storms and can be deflected by ocean currents (Ardhuin et al., 2017; Gallet & Young, 2014; Munk et al., 1963; Munk & Snodgrass, 1957). These impacts will be discussed together with other caveats of these simplifications by utilizing different conceptional models to reveal interactive atmosphere-ocean-ice processes.

3. Methods

3.1. Seismic Data

The Ross Ice Shelf Vibration Project was a field campaign from October 2014 to December 2016 with the goal of recording the response of the RIS to gravity waves for geophysical, glaciological, and oceanographic purposes (Bromirski et al., 2015). A network of 34 seismic stations recorded two years of continuous three-directional displacements at each station. The three front stations are used for the analyses in this paper.

Figure 2a shows the spectrogram of the vertical displacement at DR01 for about two months. The most common features are sloped lines of anomalously high wave activity in the swell band. These are dispersed arrivals of ocean swell at the ice shelf.

3.2. Model Optimization

Hell et al. (2019) developed a method to catalog these dispersed swell arrivals (swell events) using a two-stage optimization procedure. Here we give a brief overview of the model function, the optimization method, and the uncertainty estimation.

3.2.1. Model Function

The model function is constructed to mimic the dispersion slope of the swell as well as its characteristic shape in frequency and time. It is chosen because it allows an effective separation of storm-induced signals from those that might be induced by other mechanisms (like iceberg calving) that are also observed by the RIS seismometers. The model function has six free parameters that determine its shape and two that determine its slope (Figure 1b).

In frequency, the model function employs the JONSWAP spectrum (Hasselmann et al., 1973), which is similar to the Pierson-Moskowitz spectrum for a fully developed sea (Pierson & Moskowitz, 1964). The use of a parametric wave model as a functional form for the swell arrivals has the advantage of potentially reducing the model-data misfit. It incorporates prior physical knowledge in the optimization procedure, which is an advantage compared to other generic “machine learning” approaches.

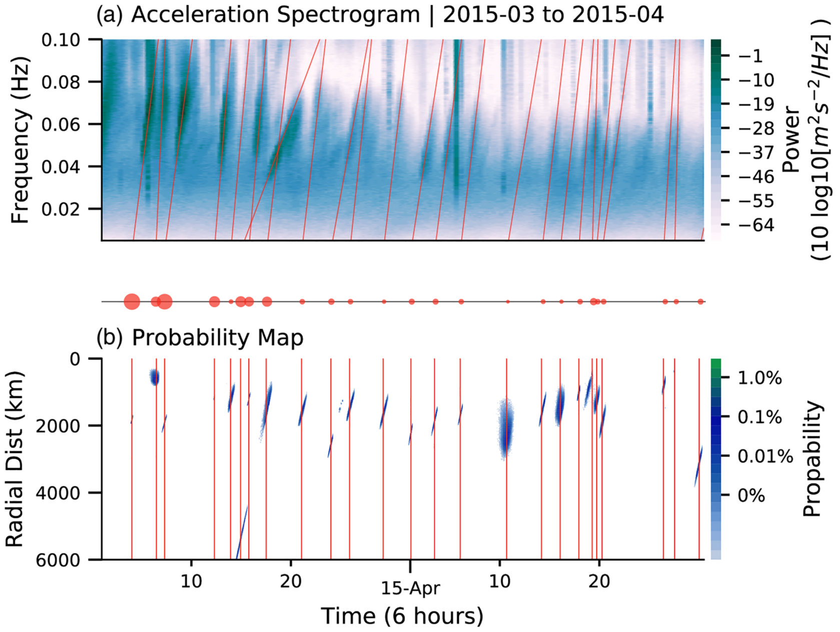

Figure 2. (a) Seismic spectrogram of the RIS response to gravity waves. The red lines show the optimized dispersion slopes for events from the Southern Ocean. (b) Probability maps of wave origins in radial distance and time for the same time interval as (a). Here, the red lines indicate the best guess of initial time, that is, when the lines in panel (a) are projected to cross the 0-Hz line. Each elliptic pattern in (b) is the probability distribution of the corresponding wave event in (a). The smaller the probability patterns, the more certain the wave event origin is. The red dots between both plots are proportional to the estimated swell amplitudes for each event at the initial time.

In the time domain, the model used the Γ distribution to account for the sharp leading edge of the incident wave events. Both functional forms incorporate a linear trend to account for the change of peak frequency with time (equation (2) and Figure 1b).

After a preliminary step in which each swell event is isolated, a cost function is constructed as the difference between model and data, weighted by the geometry. In addition, lasso-regularization is used to avoid extremes in the parameter space (Hell et al., 2019).

3.2.2. Optimization Method and Estimations of Uncertainty

The nonlinear model is optimized using a two-stage fitting algorithm to minimize the difference between model and data. In the first stage, the model is initialized with a set of parameters, which are then refined using the Levenberg-Marquardt Algorithm (damped least squares; Newville et al., 2014) to find a local minimum of the cost function. The Levenberg-Marquardt algorithm calculates the local cost function gradient in parameter space and moves its next guess of parameters in the direction down the gradient.

In the second step, a Parallel Tempering Markov-Chain-Monte-Carlo (Earl & Deem, 2005; Foreman-Mackey et al., 2013; Goodman & Weare, 2010) method is used to further minimize the cost function and produce a posterior error distribution for all variables simultaneously. This process is similar to simulated annealing, where the progress toward an optimal solution can only be seen from the average of many iterations rather than from each single iteration (Kirkpatrick et al., 1983). This is a powerful tool in situations in which multiple optimal solutions could exist. Even though one origin per wave event is assumed, the uncertainty estimate from Parallel Tempering Markov-Chain-Monte-Carlo is generally capable of capturing several wave events that arrive at the same time. The uncertainty in parameter space is inferred by sampling the posterior probability density using the data-model difference (a likelihood function based on an L2-norm) and a prior distribution generated by a random walk process (Foreman-Mackey et al., 2013). The uncertainty distributions of the two slope parameters are converted into a joint probability distribution of radial distance and time. An overview of the resulting initial times and radial distance, as well as the corresponding errors, is shown in Figure 3.

Incident wave events are observed at all three stations at the ice shelf front nearly simultaneously, but the quality of the optimization procedure varies between the stations due to independent noise. Hell et al. (2019)

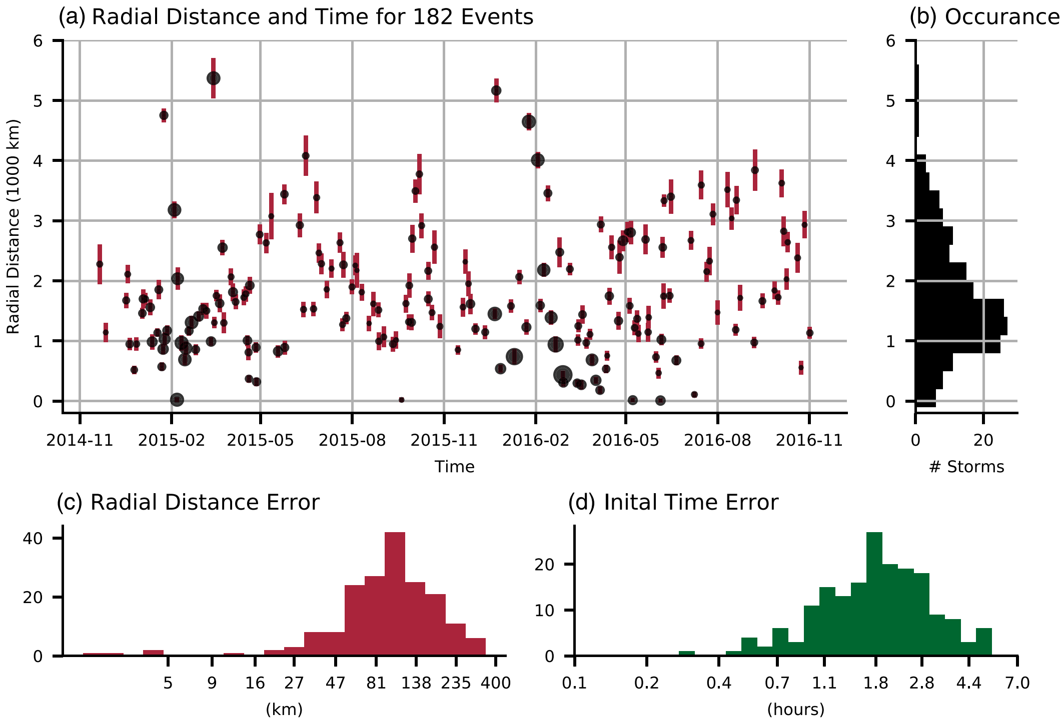

Figure 3. (a) Estimated radial distances and initial times for the 182 wave events from Southern Ocean storms. Black dots show the event radial distances and initial times, while their sizes indicate the observed amplitudes. The vertical red lines show two standard deviation of the uncertainty of the initial time inferred from PTMCMC (section 3.2.2). (b) Histogram of number of storms per radial Distance (c) Histogram of radial distance error and (d) initial time error.

selected the best fitted model for each case between the three stations nearest the ice edge. Wave arrivals that have a more complex generation history, such as two swell events observed at the same time or swell that is generated by more than one system, have a larger fitting error and are neglected from the analysis (see definition of the fractional error in Appendix A). The derived data set contains 182 incident wave events originating from the Southern Ocean. In Figure 3a, each dot represents the estimated radial distance and initial time of an observed and successfully fitted wave event. The red bars indicate radial distance uncertainty, and the dot diameter illustrates the observed amplitude of the events. Most of the events have radial distances that coincide with the Southern Ocean storm track ($1–2\times10^3$ km; Figure 3b). The median estimated error is about 110 km in space and 2 hr in time (Figures 3c and 3d).

3.3. Cyclone Detection

For cyclone tracking and surface wind fields, we use two reanalysis products: Modern-Era Retrospective analysis for Research and Applications, Version 2 (MERRA2) and ERA5 (Global Modeling and Assimilation Office, 2015a, 2015b; Gelaro et al., 2017; Copernicus Climate Change Service Climate Data Store, 2017). These are selected because they provide hourly fields, while many other reanalysis products are released at 6 hr or daily time intervals. The 2 hr and 110 km uncertainties from the optimization method imply that hourly wind fields are needed to compare with observations (Hell et al., 2019). The two reanalysis products rely on similar sets of observations and have comparable overall statistics (Wang et al., 2016). By using two products, we are able to assess cases in which the representation of extratropical cyclones differs (Hodges et al., 2011).

In our assessment of reanalysis storm tracks, first, the reanalysis sea level pressure (SLP) is regridded to a 50-km equal area grid (Equal-Area Scalable Earth Grid) EASE-Grid in the Southern Hemisphere (M. J. Brodzik et al., 2012; M. Brodzik et al., 2014), and second, a cyclone detection and tracking procedure is applied to the 1-hourly fields (Crawford & Serreze, 2016, 2017). Our algorithm uses the evolution of SLP rather than the often used 850 hPa vorticity, but the results are expected to be very similar (Hoskins & Hodges, 2002, 2005; Hodges et al., 2003; Neu et al., 2012; Simmonds & Rudeva, 2014; Simmonds & Keay, 2000). Compared to vorticity tracking, this algorithm provides a more direct relation to surface winds,

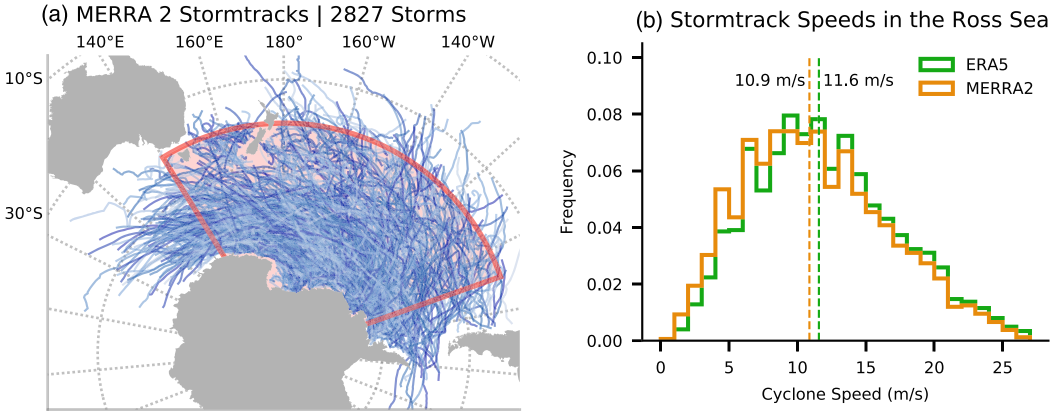

(c) Snapshot on 2015-07-16T11:30

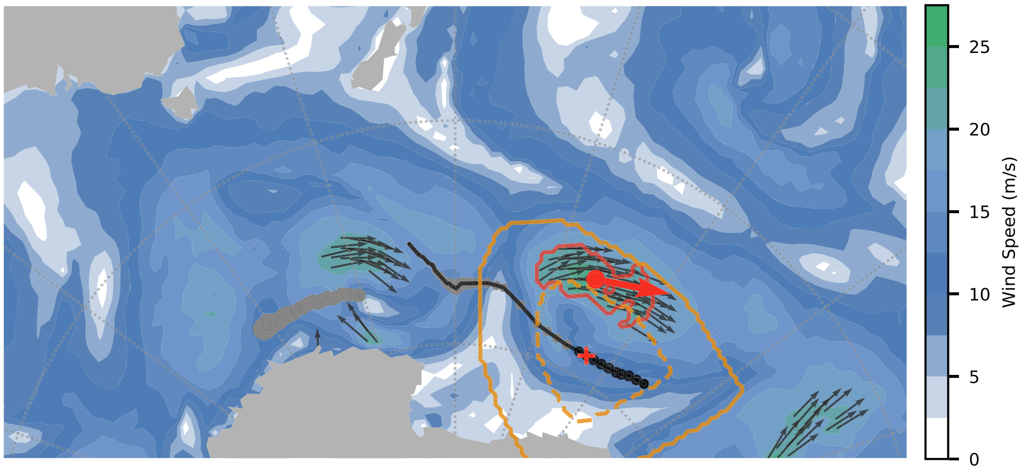

Figure 4. (a) Storm tracks from MERRA2 between October 2014 and December 2016 that are longer than 100 km and last longer than 4 hr in the red area. Data points near the coast are excluded. (b) Probability density function of cyclone propagation speeds in the Pacific sector of the Southern Ocean derived from ERA5 storm tracks (green) and MERRA2 storm tracks (orange). (c) A snapshot of an extratropical cyclone with the black line indicating its individual storm track in July 2015. The orange dashed contour is the outer closed sea level pressure contour of the storm track during that highlighted time step and the solid orange contour is the cyclone area, which is the graphically widened closed contour. Patterns of high wind speed that exceed the wind speed 90th percentile ($\approx$16 m s^{-1}) in this area are marked with a red outline, and black arrows indicate the wind direction for these 90th percentile winds. These are used to define the fetch area. The red dot and arrow show the center and mean wind direction of these patterns, while the red cross indicates the center of the cyclone at the chosen time step. The shading shows the wind speed in meters per second.

smoother fields, and additional analysis fields used to identify wind fetches (next section). In previous studies, storm tracking algorithms have typically been applied to 6-hourly or daily time steps; comparisons on a case-by-case basis generally show good agreement between storm tracks from 1- and 6-hr fields of the same reanalysis (Blender & Schubert, 2000).

At each time step the minima of SLP are identified and connected to minima in the previous time step. The resulting cyclone tracks are masked out over land or ice shelves and rejected if they are in the Indian or Atlantic sectors, or if they have a lifespan shorter than 24 hr or a length shorter than 100 km. All remaining cyclone tracks between October 2014 and December 2016 are shown in Figure 4a. Each line shows the spatial evolution of a storm track, defined as the time-evolving location of the surface pressure minimum of an extratropical cyclone.

Figure 4b shows the distribution of storm translational velocities in the Pacific sector of the SO. The median translational velocity is about 11 m s^{-1}. Based on this, we use 10 m s^{-1} as a simple estimate to convert between spatial distances and time periods (section 4.1).

3.4. Fetch Detection

Each storm has areas of strong surface winds. They are often associated with warm or cold fronts (Beare, 2007; Doyle, 1995; Munk, 1947; Neiman & Shapiro, 1993) and found at radial distances from the pressure minima that are roughly aligned with the largest closed contour of SLP around the local pressure minimum (Figure 4c, orange dashed line, Bengtsson et al., 2009; Hodges et al., 2011). These areas of strongest winds under a cyclone are also areas of high surface stress (Adamson et al., 2006; Beare, 2007; Hasselmann et al., 1973) and therefore intensified wave generation. We identified these “fetch areas” using the following procedure:

As indicated in Figure 4c, first, the cyclone area (solid orange line) is defined as twice the area of the last closed SLP contour (dashed orange line) for each storm track (black thick line) and time step. Second, fetches are identified by searching for patterns that exceed the 90th percentile of the wind speed distribution under the cyclone area (red outline and black arrows in Figure 4c). As a practical approach to defining fetch area, only patterns larger than 16 grid points (40×10^3 km^2) are kept and used as a practical definition of fetch areas (Figure 4c, red contours). Cyclones can have several fetches at each time step, and fetch centers are generally displaced a few hundred kilometers from the cyclone centers (compare red dot and cross). This pattern identification allows us to evaluate the evolution of fetch areas under cyclones over time and to draw inferences about reanalysis product performance on the scale of fronts rather than on the scale of cyclones.

4. Results

4.1. Matching Reanalysis Storms With Observations

To obtain the storm locations in the Southern Ocean from the seismic swell observations, we examine each of the observed events and compare them to the reanalysis storm tracks. The estimated dispersion slopes and uncertainties in observed swell arrivals are converted to two-dimensional probability density distributions of initial time t_0 and radial distance r_0 (Figure 2b; Hell et al., 2019; Munk, 1947). Swell statistics inferred from the seismic data provide direct information about wave origins (cf. Figures 2a and 2b). Smaller patches of high probability density correspond to more certainty in wave origins. Large patches of high probability represent either deficits in the model optimization or just larger possible regions of wave generation. This section explains how a likelihood map of wave origins is used to determine wave generation regions in the Southern Ocean.

To compare the derived likelihood maps with the identified fetches (section 3.4), storm tracks and fetches are remapped in the same space as the likelihood maps. The remapping is illustrated in Figure 5 with black lines showing an individual storm track and orange dots identifying fetch area in latitude-longitude space (Figures 5a, 5c, and 5e) and radial distance and time space (Figures 5b, 5d, and 5f). We calculate the radial distance of each storm position and fetch area to the observation site (blue dots on the RIS in Figures 5a, 5c, and 5e) at each time step for all storms and fetches, such that there is one-to-one correspondence between estimated distances and reanalysis winds. This reduces the spatial dimensions to the radial distance between the location of the storm and the observation site on the RIS. Consequently, the red semicircular arcs in Figures 5a, 5c, and 5e map to horizontal lines in Figures 5b, 5d, and 5f and can be used for orientation. In a next step, the orange center points of all tracked fetches under storms are compared to the likelihood maps (black shading in Figures 5b, 5d, and 5e). Each of these fetch points i is matched with the observation-based probability by finding

$$p_{match} = \max \left\{ p_i \tilde{X}_i \right\} \quad \cap \quad p_i > 0.1\%, \tag{3}$$

where p_i is the underlying probability of the fetch i at its time and radial distance and $\tilde{X} = f_m U_{10}/g$ is the nondimensional fetch as a measure of the wave generation based on the mean wind speed over the area of storm-related high winds from reanalysis (Hasselmann et al., 1973). This is illustrated in Figures 5b, 5d, and 5f for MERRA2 winds (the same events for ERA5 can be found in the supporting information). For this likelihood map, the green dot is the fetch where (3) is maximized relative to all N fetches and the orange dots also belong to this identified storm track (black line) but occur at time steps before or after the matched fetch. Only well-identified storm tracks and fetches are shown (see section 3.4). Once identified, the time evolution of the identified storm track and fetches can then be displayed in latitude-longitude maps (Figures 5a, 5c, and 5e) together with estimated radial distances (red lines). Note that (3) does not require an identified fetch to align with the probability maximum p_{max}. The distance between the most likely origin p_{max} (blue cross) and the matched origin p_{match} (green dot) is shown as a blue line in Figures 5b, 5d, and 5f.

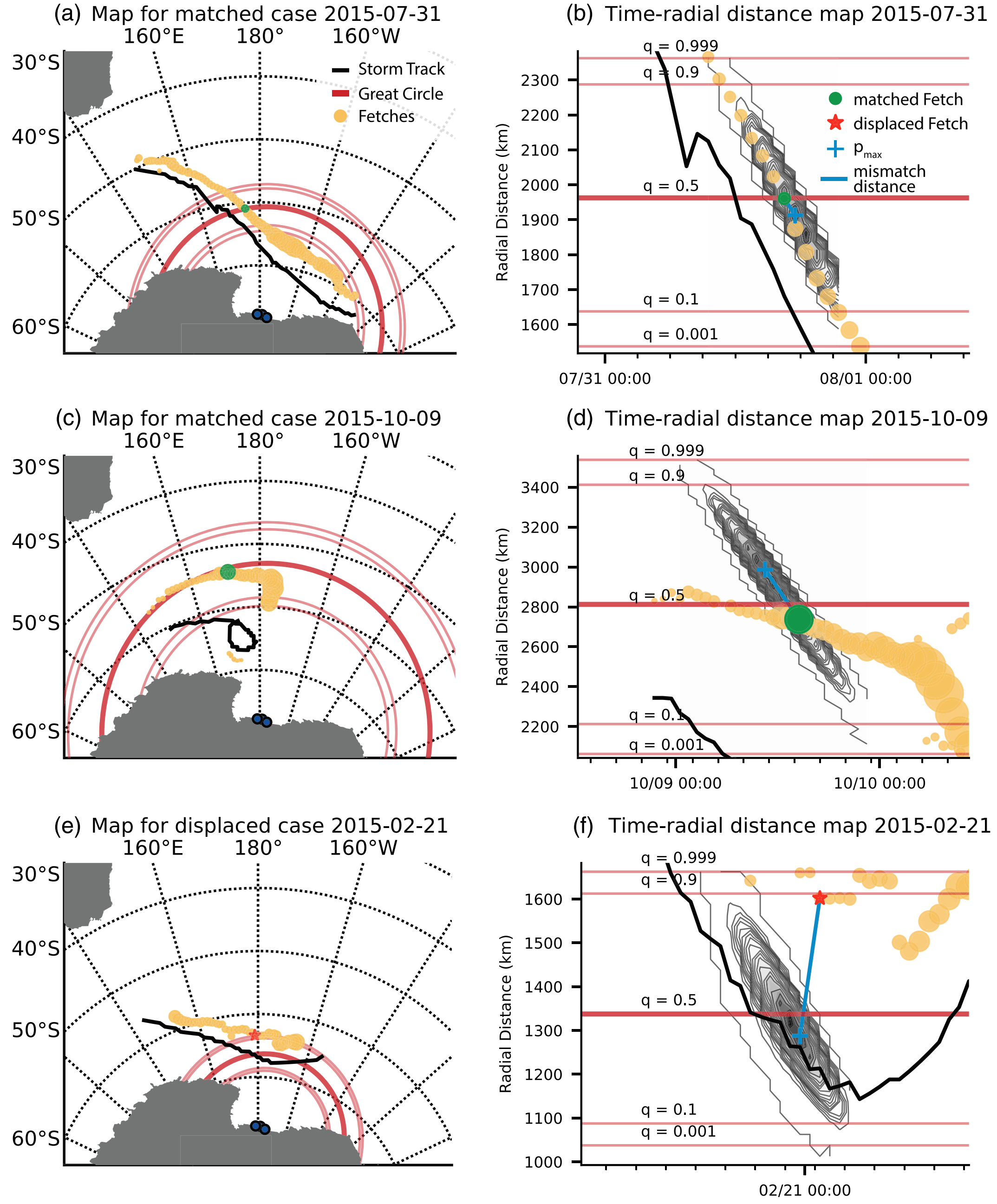

Figure 5. Examples of the matching procedure in latitude-longitude space (a, c, and e) and associated radial distance and time (b, d, and f) for MERRA2 winds. (a and c) The event's storm track is in black, and associated fetch locations are shown as orange dots, with the dots sizes indicating the nondimensional fetch size $\tilde{\chi}$ (section 4.1). The green dot indicates the matched fetch location (3), as illustrated in (b), and the red lines show the 0.1th, 10th, 50th, 90th, 99.9th percentiles of the radial estimate. (b and d) Illustration of the matching procedure with the storm track in black, its fetches in orange, and best identified fetch in green. The distance from the identified fetch (green dot) to the maximum likelihood p_{max} (blue cross) is shown as a blue line. The red lines indicate the same radial distance estimates as in (a) and (c). Black contours show the likelihood maps generated by Monte Carlo sampling (section 3.2.2). (e and f) Same as (a) and (b) but for a case that does not fulfill the matching condition. The best fitted fetch is shown as a red star. Observation positions on the RIS are shown as dark blue dots with black circles in the left panels.

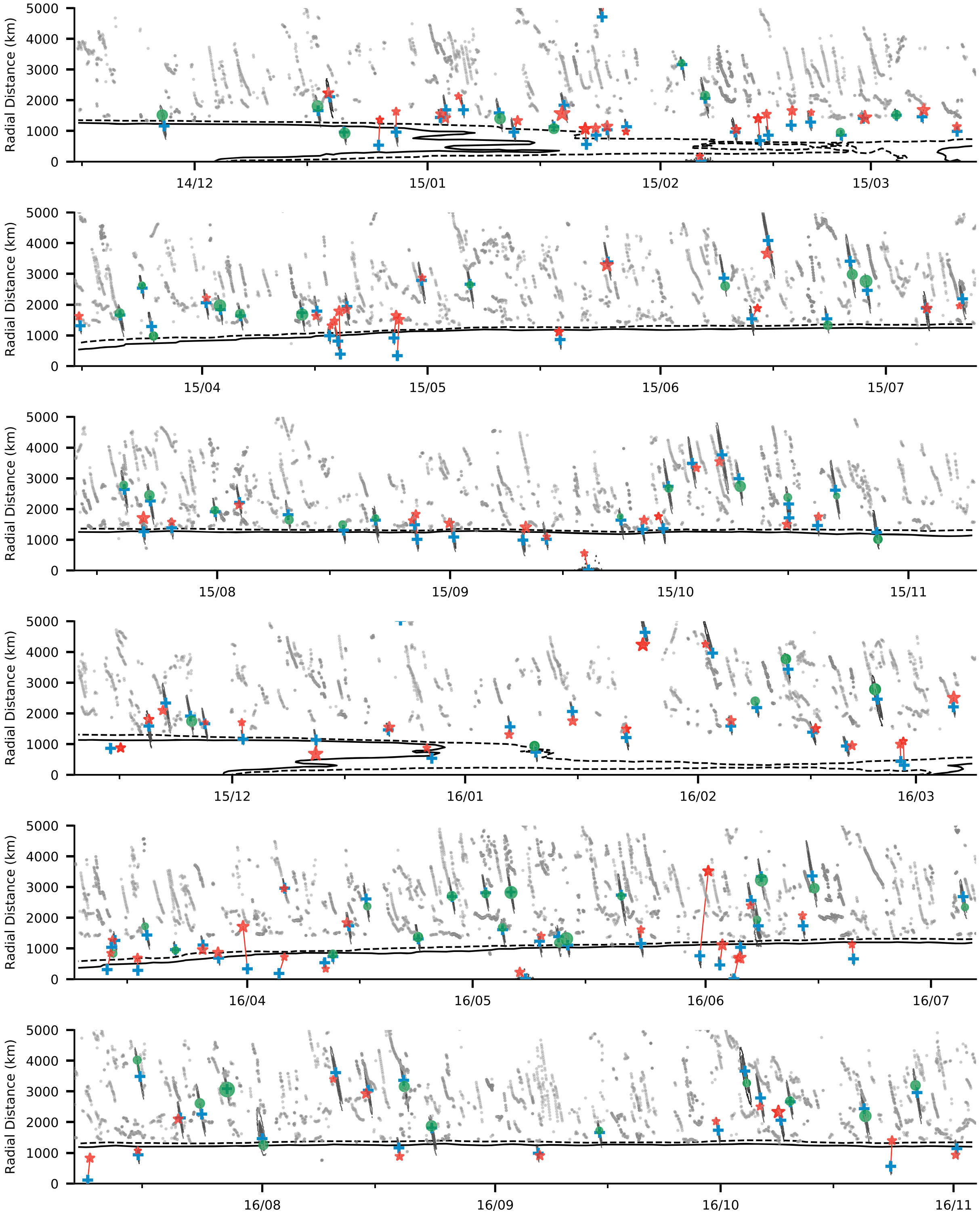

Figure 6. All observed wave events remapped in the time and radial distance domain, with each panel spanning about 4 months. Green dots and red stars indicate matched or displaced fetches, respectively, and the green or red lines show the distance (5) to the probability maximum p_{max} (light blue cross). The black stripes are the likelihood patterns as in Figure 5. The black and dashed lines show the 20% and 50% sea ice concentration in the same coordinate system (data from Toudal Pedersen et al., 2017), and the gray dots indicate the position of all possible fetches derived from the fetch detection algorithm (section 3.4).

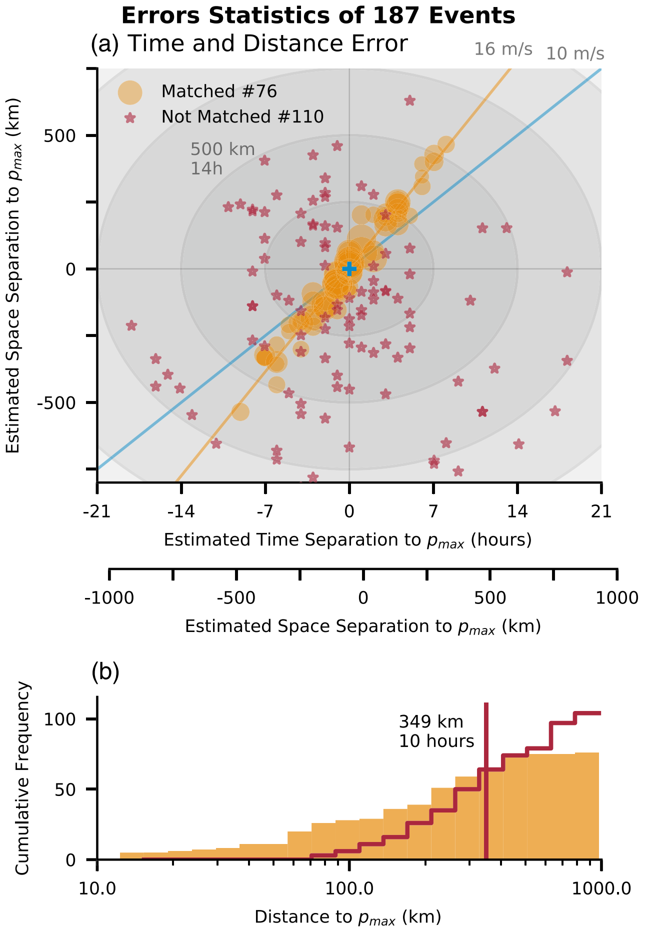

Figure 7. (a) Spatial and temporal bias relative to the probability maximum of matched (orange dots) and displaced fetches (red stars). The size of the orange dots indicates the probability from the PTMCMC with which they have been matched, and the orange line shows a least squares fit to all matched cases. The gray circles are lines of constant spatial-temporal error in 500 km/14-hr intervals, because a time difference of 14 hr is converted to a spatial distance of about 500 km using an average cyclone speed of 10 m s^{-1}, indicated by the blue line, while the fitted slope of all matched cases (orange dots) is show with the orange line (16 m s^{-1}).
(b) Cumulative density function of matched (orange) and displaced (red) fetches. The median bias of displaced fetches is about 349 km or ≈10 hr equivalently.

If (3) is not satisfied, that is, there is no probability >0.1% assigned to any of the N wind fetches, the fetch with the minimal distance d_i between the highest probability p_{max} and the fetch position is selected using

$$\min\left\{d_i\right\}, \tag{4}$$

with

$$d_i = \left(\left[r_0(p_{max}) - r_{0,i}\right]^2 + \left[(\quad t_0(p_{max}) - t_{0,i}) \quad U_c \quad\right]^2\right)^{1/2}, \tag{5}$$

where $U_c = 10$ m s^{-1} is an average cyclone speed estimated from the observed cyclone tracks (section 3.3Neu et al., 2012). Cases where condition (3) is not satisfied will be called *displaced* throughout the paper, and their displacement is estimated by condition (4). Figures 5e and 5f shows an example of an identified event of this kind. The red star identifies the fetch area using (4), and the blue line is the calculated distance using (5). Although there are fetch areas within the estimated radial distance (Figures 5e and 5f), they occur at the wrong time to explain the seismic observations (more examples in the supporting information). Similarly, there are fetches that occur at the right time, but not at the appropriate radial distances. This separation between temporal and spatial displacement is only possible because of the correlated uncertainties in radial distance and initial time (Figures 5b, 5d, and 5f, black contours) that are derived from the uncertainty estimation (section 3.2.2). The correlated uncertainty represents the ambiguity between a wave event originating earlier from a distance r_a and a wave event originating later from a distance $r_b < r_a$. A detailed description of the underlying parametric model and the error estimation procedure is given by Hell et al. (2019).

The resulting matches between fetches and likelihood maps are shown in Figure 6 for MERRA2 and in Figure S6 for ERA5. The color convention is the same as in Figure 5: Matched fetch positions are indicated by blue dots, positions of displaced fetches as red stars, and the likelihood maps are in black contours with their maxima emphasized with blue crosses. The distance between the likelihood maximum and the associated fetch is indicated by a red or blue line, respectively.

While there is a predominant radial distance from wave origins to seismic stations (about 1,500 km), we do not see a systematic difference between matched and displaced events over time nor do we identify a difference that is associated with larger or smaller likelihood maps. The gray dots in the background show all possible fetches that each observed event was compared to and illustrate that even random pairs of radial distance and initial time might overlap with estimated fetch positions. However, the physical constraints on the optimization model and the uncertainty estimates give us confidence that the likelihood maps describe wave event origins that have more skill than random guesses. The large number of possible point sources as wave origins and the small fraction of observed discrete wave events shows that the concept that waves originate from point sources is oversimplified (Munk, 1947), because many of the identified point sources belong to the same dynamical system; that is, separate fetches under the same storm can together do continuous work on the ocean surface and are jointly responsible for swell wave generation by nonlinear wave-wave interactions under the storm (Hasselmann et al., 1985). For simplicity, we treat fetches under a storm as independent point sources at each time step, even though we know they are not. However, this assumption of independence allows us to make a leading-order evaluation of the reanalysis surface wind positions.

The sea ice concentration is also remapped in the same coordinate system and is shown as dashed (20%) and solid black lines (50%) in Figure 6. Visual inspection suggests that wave origins in sea ice or near the sea ice edge are more likely to be displaced than open ocean events (see section 4.2).

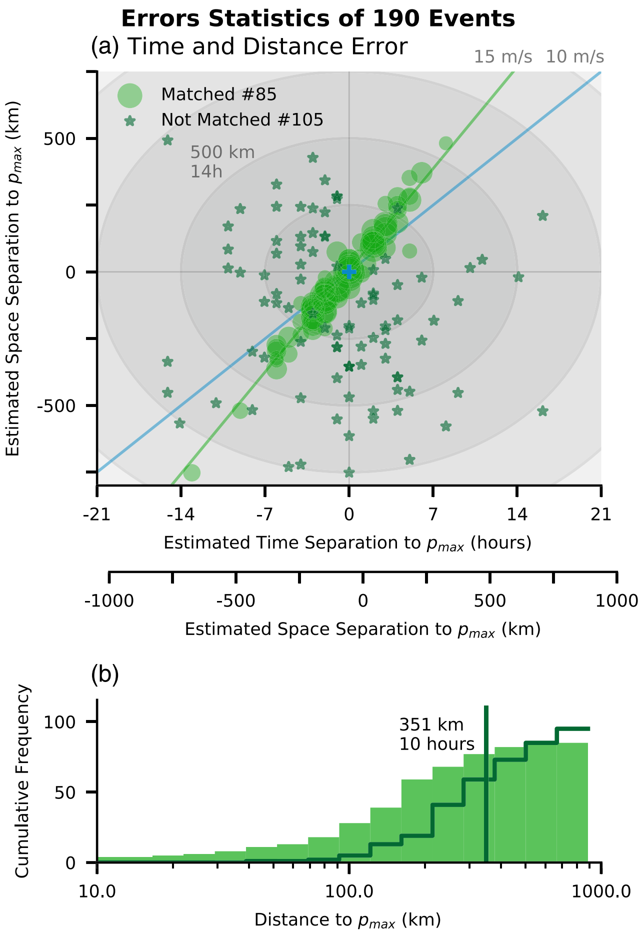

Figure 8. Same as Figure 7 but for ERA5 with matched cases in light green and displaced cases in dark green.

We also note that there are clearly cases with unrealistically distant fetches (Figure 6 at the end of March 2016 and at the end of May 2016). Reasons for this can be multi-fold. The reanalysis winds over land instead of over the ocean would not generate swell, and therefore should be excluded from this analysis, or the actual wind event that generated the swell simply might not exist in the reanalysis product, perhaps because the wave origin is in the region of sea ice.

Because the estimated uncertainties and displacements are small, all cases shown in Figure 6 are remapped into a coordinate system centered at the probability maximum p_{max} (Figure 7 for fetch derived from MERRA2 and Figure 8 for fetch derived from ERA5). Again, dots indicate matched cases ($p > 0.1\%$), that is, when the fetch identified from reanalysis is consistent with the storm arrival at the seismic station. This includes high probability cases centered at p_{max} and also lower probability cases that align along a 16 m s^{-1} line (fitted orange or green line in Figures 7 and 8). As a result, origins that are shifted by 15 m s^{-1} in space and time from p_{max} are matched, even though they are displaced, due to the correlated uncertainties in t_0 and r_0. Also note that the estimated average shift of 16 m s^{-1} for matched cases is faster than the assumed storm speed of 10 m s^{-1}. Stars show displaced cases, identified by condition (4), in which the time and position of the fetch origins are not consistent with the swell arrival at the seismic stations. These cases may be similar to the consistent cases in terms of their distance to p_{max}, but they are judged to have physically implausible surface wind positions. This distinction between matched and displaced events is justified by the shape of the estimated uncertainties (section 3.2; Hell et al., 2019). An independent assessment of the spatial and temporal error would lead to a two-dimensional Gaussian-like uncertainty. This independent error assessment would fill a much larger area in the parameter space of Figure 5 or Figure 6 than a correlated error. The combined error assessment used in this analysis provides much finer distinction between physically plausible and implausible cases.

For MERRA2 reanalysis, 76 storm fetches are matched with seismic station swell arrivals with a probability >0.1%; for ERA5, 85 storm fetches match. In total, of the 187 observed and well-fitted swell arrivals, for MERRA2 41% of cases have an identified match and for ERA5 45% of cases (Figures 7, orange dots, and 8, green dots). Half of these matched cases are separated from the probability maximum by less than 207 km—or 5 hr—for MERRA2 or less than 170 km—or 5 hr—for ERA5. The other half of the matched cases show larger distances to the storm center but still are consistent with the observations, because the probabilities are correlated in distance and time (Figures 2 and 5).

For more than half of the events observed at the seismic stations, the position and time cannot be linked to a high wind area under a cyclone (110 events for MERRA2 and 105 events for ERA5). This represents 59% of the observed events when matched to MERRA2 winds (Figure 7a, red stars) or 55% of the observed events when matched to ERA5 winds (Figure 8a, green stars). The median displacement of the set of displaced storms is about 350 km—or 10 hr—in both observational products (Figures 7b and 8b).

Both reanalysis products have roughly the same number of storms from which waves could originate (3,332 tracked storms in MERRA2 and 3,118 tracked storms in ERA5; Figure 6, small gray dots). However, the number of storm events observed seismically is less than the total number of south Pacific storms because not every storm generates waves that propagate toward the Ross Sea, not every event is equally well observed, and not every event has long enough waves to penetrate through sea ice. Only 6% of the storm tracks identified in the reanalyses appear to generate waves that are transmitted to the ice shelf.

Of the 187 total seismic events observed at the ice shelf, 57 (about 30% of all observed) events can be matched to both reanalysis products, 88 (47% of all observed) events cannot be directly associated with either

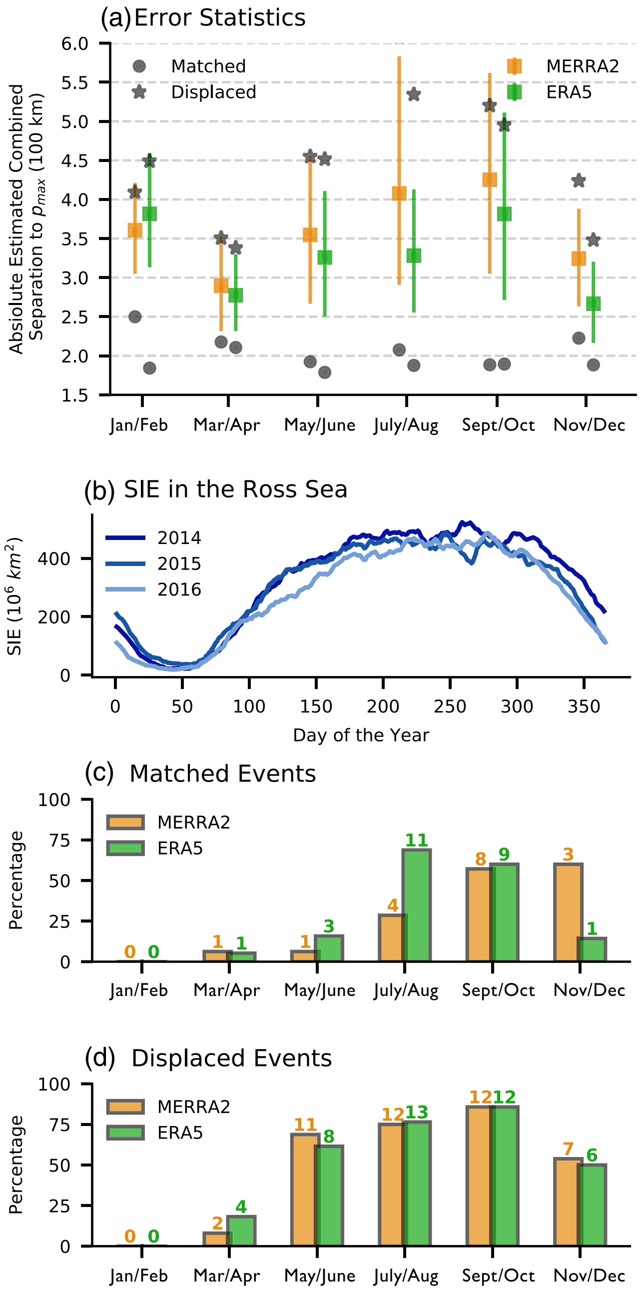

Figure 9. (a) Seasonal dependence of the distance to the highest probability p_{max} and the closest fetch in the open ocean (Figure 7a). The orange square is the bootstrapped median of MERRA2 and green represents the bootstrapped median of ERA5, in both cases for matched and unmatched cases combined. The vertical lines indicate the spread of the 5th to 95th percentile of the bootstrapped median distribution. Gray dots are the bootstrapped medians of the matched cases, and gray stars are the bootstrapped median of displaced cases, following the convention in Figures 7 and 8. (b) Sea ice extent in the Ross Sea for 2014 to 2016. (c) Percentages of all matched events in the bi-monthly period with fetches over an area with 20% sea ice concentration or more. The numbers on the bars are the total number of events meeting this criterion, while the vertical axis indicates their percentage. (d) Same as (c) but for displaced cases

MERRA2 or ERA5, and the remaining 42 observed events (23%) are matched with a fetch in only one of the reanalysis products. We hypothesize that the mismatches and inconsistencies between reanalysis products stem from the paucity of atmospheric observations available to constrain the reanalyses.

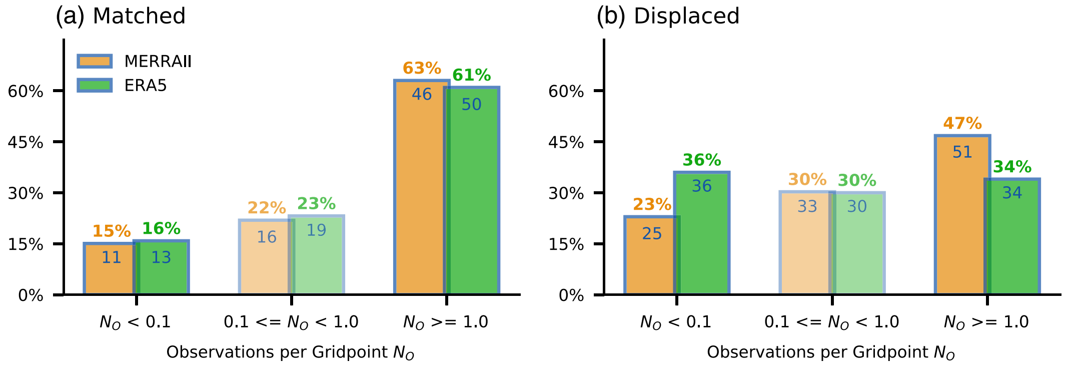

Figure 10. Available wind observations at the place and time of the identified fetch areas expressed as observations per grid point N_0. (a) Percentage of matched cases with $N_0 < 0.1, 0.1 \leq N_0 < 1.0$, or $N_0 \geq 1.0$ for ERA 5 (green) and MERRA2 (orange). Colored numbers on top indicate the respective percentage, while numbers in the bar indicate the total number of events in each category. (b) Same as (a) but for displaced cases.

4.2. Seasonal Error Dependence and the Role of Sea Ice

A potential reason for displaced winds in the reanalysis products is summarized in Figure 9. The seasonal dependence of the median radial distance error d (5) is binned in 2-month segments (Figure 9a). Distance error estimates are obtained from the distribution of the mean error for each 2-month period via bootstrapping using 10^5 repetitions (with replacement). The median of d is highest in late austral winter (September/October) and smallest at the end of summer (March/April, Figure 9, orange and green squares). This seasonal change in the median error is mainly due to displaced events (median of displaced events shown as stars in Figure 9a) and is mainly driven by displacement in radial distance rather than time (Figure S7).

The seasonal variation in displaced wind events could potentially be attributed either to seasonal change in the performance of the reanalysis products (i.e., seasonal changes in the spatial coverage of in situ or remotely sensed surface wind measurements), or to seasonal changes in the quality of the fitting algorithm. The seasonality in the distribution of d roughly follows the sea ice extent in the Ross Sea (Figure 9b), while there is no seasonal change in the quality of the model fitting (Figure A1). A comparison of sea ice concentrations with the identified fetch areas suggests that most events (up to 75%) occur over a sea ice concentration of at least 20% when the sea ice extent is largest (Figures 9c and 9d).

4.3. Available Observations at the Identified Source Locations

Displaced wind events in winter more likely originate from locations with sea ice (>20% sea ice concentration) suggesting that the reanalyses have larger surface wind biases in the presence of sea ice, because the wind retrievals by satellite or in situ observations are impeded by the presence of ice. Figure 10 shows the average number of available remote sensing observations per grid point for each of the identified high wind speed areas of matched and displaced wind events (microwave radiometers and scatterometers, taken from Atlas et al., 2011; Wentz et al., 2015). If the reanalyses are constrained by one or more satellite observations per grid point, then the fetch area is at the correct location in about 60% of the cases, but if there are essentially no observations within the fetch area ($N_0 < 0.1$ in Figure 10), then the reanalysis-derived fetch area only appears to be at the right position and time in about 15% of the matched cases, because they have no direct constraint from remote sensing winds.

In contrast, displaced cases more frequently occur when no winds are available (23–36% of cases; see Figure 10b), though they can also occur when at least one observation is available (34–47%). Fundamentally, these results suggest that both reanalysis products generate similar, dynamically consistent surface winds that are not accurate enough to explain all of the observed swell events, and that part of the challenge for the reanalysis products stems from the sparsity of satellite observations. If there is at least one wind observation to constrain the reanalysis, then the probability of finding a matched case is about 60% (Figure 10a), though the availability of observational constraints does not preclude the possibility of displaced cases (Figure 10b).

4.4. Influences of Ray Bending and Advection by Currents

Another hypothesis for why the source location estimates can be displaced from the wind areas identified in reanalyses stems from bending and advection of swell waves due to currents. As we will show in this section,

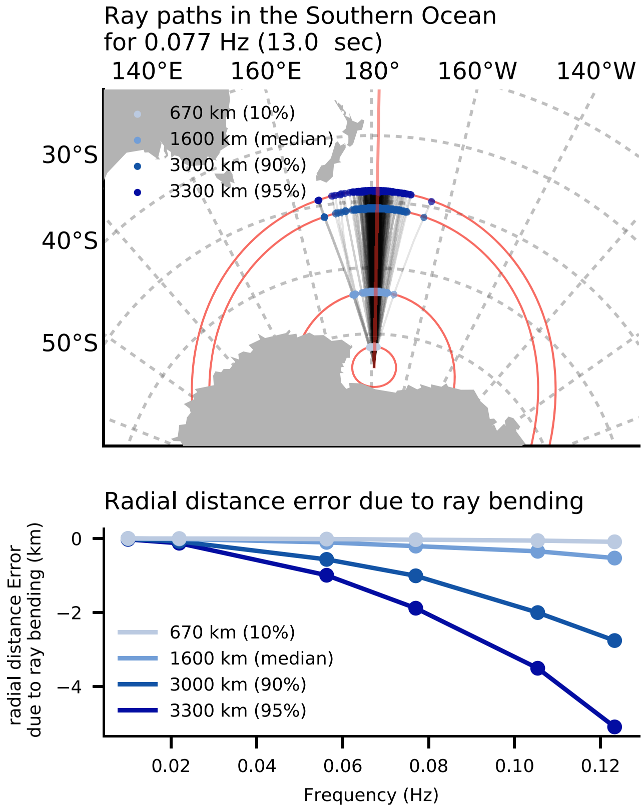

Figure 11. (top) Ray paths for waves with a 13-s period (0.077 Hz) that propagated through surface currents. Each ray is propagated from a point near the ice shelf edge through a 5-day mean surface current field obtained from a (1/12)° SOSE run (Erickson et al., 2016). The blue dots show the end points for a given length (760, 1,600, 3,000, and 3,300 km from the seismic stations at the ice shelf edge), and the red circles are the great circle equivalents. (bottom) Median deviation of the ray's end points to the defined great circle distance.

both processes are negligible for this analysis. To assess the deviations that raypaths might experience due to currents, we used 5-day mean surface current fields from a (1/12)° free model run configured for the Southern Ocean State Estimate (Erickson et al., 2016).

Rays were propagated using the ray equations for advecting and bending surface waves (Gallet & Young, 2014; Munk et al., 1963) from the Ross Sea northward for each of the available 488 model time steps (6 years and 8 months). Figure 11 top shows the ray positions for several travel path lengths (670, 1,600, 3,000, and 3,330 km corresponding to the 10th, 50th, 90th, and 95th percentiles of the estimated distances from the Southern Ocean to the RIS; see Figure 3b). The spread of ray positions for fixed ray length grows with the path length, but importantly, this spread in longitude and latitude does not add to the uncertainty in radial distance. It shortens the path length only marginally, even though the latitude-longitude positions can change substantially.

The advection of rays by the currents is also negligible for typical current speeds U of about 0.3 m s^{-1} and even for slow waves (0.1 Hz) with group velocities of about 7.8 m s^{-1} eq. (2), such that $U \ll c_g$ is true most of the time (Gallet & Young, 2014). Only eddy-scale current speeds (e.g., $U \approx 1.5$ m s^{-1}) can significantly alter the path of shorter waves. However, since Southern Ocean eddies are small, not surprisingly the advective impact on ray paths is small compared to ray bending in this error analysis (Rocha et al., 2015).

The two spatial dimensions are collapsed to a great circle distance by the matching analysis (section 4.1). The analysis treats all great circle distances equally, regardless of their angle to the station (or latitude-longitude position). Consequently, ray bending can only contribute to the great circle distance uncertainty if it substantially changes the great circle distance for a given path length.

The systematic overestimation of the great circle distance when assuming great circle paths is expressed as the *radial distance error due to ray bending*. It is defined as the distance of the ray end points from the great circle distance line that has the same path length as the ray (Figure 11, red line). The median error is proportional to the wave frequency and the ray distance (Figure 11, bottom). For the frequency range in the above analysis (0.02 to 0.1 Hz) the ray bending effect is rather small. Even the shortest waves (≈0.1 Hz) from the most distant Southern Ocean storms (3,300 km) have a *radial distance error due to ray bending* that is smaller than 4 km. This is less than 4% of the typical uncertainty in the great circle distance estimation derived from the RIS observations (≈110 km; sections 3.2 and 3.2.2).

5. Discussion

We have demonstrated that Southern Ocean storms can be observed by seismic data on the Ross Ice Shelf. Detailed comparisons of the observations with two reanalysis products suggest that slightly less than half of wave events have an origin in the open ocean that is also captured by the reanalysis product (about 41% in MERRA2 and 45% in ERA5). In the majority of cases (59% for MERRA2, 55% for ERA5) the observed wave events have an equivalent high wind episode in the reanalysis that is displaced by on average about 350 km or 10 hr relative to the seismic observations. The partitioning of the time and distance component of the displaced wind events to these error estimates depends on the choice of the translation velocity of the storm. Here we assume an average velocity of 10 m s^{-1} (section 3.3; Neu et al., 2012). However, the number of matched storm events does not change with the choice of the translational velocity.

Detailed analysis of biases suggests errors in the representation of Southern Hemisphere cyclones in reanalyses. The direction and timing of cyclone displacement appear to be random (Figures 7 and 8). The displacement length is longer in winter, likely connected to the presence of sea ice (Figures 9a and 6). Generally, displaced events are more likely to occur with sea ice close to the wave generation region, while the quality of the fitting model is unaffected by sea ice (Figure A1).

We suggest that in many cases the inaccuracy of high wind events over the Southern Ocean is due to lack of available wind observations that can be assimilated in the reanalysis models (section 4.3). While satellite wind observations over the Southern Ocean are generally sparse, they are effectively nonexistent over sea ice, where no winds can be retrieved from remote sensing observations (section 4.2 and Figures 6 and Meissner & Wentz, 2009). The lack of observational constraints over or near sea ice would easily cause the resulting reanalysis to deviate from the (underobserved) true winds.

We showed that the major impact of sea ice in this analysis is that it prohibits wind observations, rather than distorting the observed wave event on its travel path. Sea ice attenuates higher-frequency swell (Ardhuin et al., 2016; Bates & Shapiro, 1980; Chen et al., 2019; Hell et al., 2019; Squire & Allan, 1980; Squire, 2007; Stopa et al., 2018), while wave dispersion changes are minor for typical mean sea ice thicknesses of about 1.5 m in the Southern Ocean Gyres and for periods longer than 15 s (Wadhams & Doble, 2009; Williams et al., 2015). This analysis only uses the dispersion of linear deep ocean waves, so the attenuation of waves in sea ice has no effect on the analysis, as long as wave-induced signals are detected by seismometers. This implies that seismic data could be part of an observing system strategy for remote detection of Southern Ocean storms by swell wave dispersion (Figure 6 and Figures 9c and 9d).

We tested the robustness of the estimated displacements against influence of ray bending due to ocean currents and concluded that the estimated storm location/timing uncertainties are not influenced by ray bending, because the error of the radial distance estimate due to bending does not exceed 4% of the typical error estimates for the great circle distance.

Additional sources of error are limitations of the cyclone detection and tracking algorithm used here (Crawford & Serreze, 2016, 2017). Although this algorithm's performance is comparable to others (Crawford & Serreze, 2016), its application to 1-hourly data rather than 6-hourly data introduces more noise to the time series of SLP fields. This accentuates errors in cyclone position and especially area, which is sensitive to interference by storms in close proximity (Wernli & Schwierz, 2006). Since our analysis relies on the position of high wind speed areas close to the cyclone, rather than the cyclone center itself, this is a minor source of error. Additionally, we accounted for the uncertainty in the storm track position by extending the area used to identify high wind speed fetches beyond the smallest closed SLP contour (section 3.4). Tests of case studies did not show sensitivity of the high wind speed positions to the chosen cyclone area past a widening factor of 2.

In addition to providing context for evaluating shortcomings in local weather forecast skill, results of this study also have consequences for wave predictions. Wave climates across the Pacific are influenced by remote swell from the Southern Ocean (Bromirski et al., 2013; Villas Bôas et al., 2017), and biases in the position and timing of Southern Ocean swell generation events directly convert to biases of local swell wave forecasts (Bidlot et al., 2002).

We do not include analysis of wave direction in the parametric model (section 3.2), because the important parameters for estimating the source locations are peak frequency and dispersion, which are invariant along the directional spread (Delpey et al., 2010). We also do not include the reanalysis wind direction in the matching criteria, because it is secondary to the radial distance criterion. If reanalysis winds are biased in their position, they are also biased in direction, such that a wind direction criterion will only further decrease the number of matched cases. In fact, since each high wind event is treated as a point source that radiates waves in all directions, the defined matching criterion (3) can find cases of reanalysis winds pointing away from the Ross Ice Shelf. Given the scant number of observed cases, we decided not to further subdivide the analysis. Thus the estimates of matched case (41% to 45%) found here should be understood as an upper bound.

This analysis uses the concept of point sources that generate ocean swell originating from the center of the high wind speed area (Munk, 1947), while a wave event observed on the RIS is typically a superposition of several of these point sources (Figures 1 and 5). We used a simple point-source conceptual model to identify a single source point as the origin of the wave energy, though we recognize that the waves could have a more complex origin. Although the sparsity of wind observations is undoubtedly one challenge, a possible further explanation for the high fraction of displaced wind events stems from the shortcomings in the point-source model, which assumes that waves originate from the point in the center of the high winds. This model might be justifiable when seeking a plausible pairing between observed wave events and reanalysis storms, but it falls short in representing all of the complexity involved in the generation of swell by an area of high wind speeds that is moving at speeds similar to the wave group velocities.

Appendix A: Seasonal Dependence of the Fractional Error

The quality of the model fit is assessed by deriving the fractional error of the model fit. The fractional error is defined as

$$e_{\text{frac}} = \frac{J_d}{\sum_{i}^{N} D_i^2 \quad w_i^2}, \tag{A1}$$

with J_d as a cost function based on the difference between data and model, D_i the data, and w_i the specific weight for each point (see Hell et al., 2019). A good model fit (i.e., low fractional errors) results in a small fractional error, while a bad model fit results in a larger fractional error. In this paper we only use observed events with $e_{frac} < 0.6$. Figure A1 shows the seasonal change of the fractional error and its running mean.

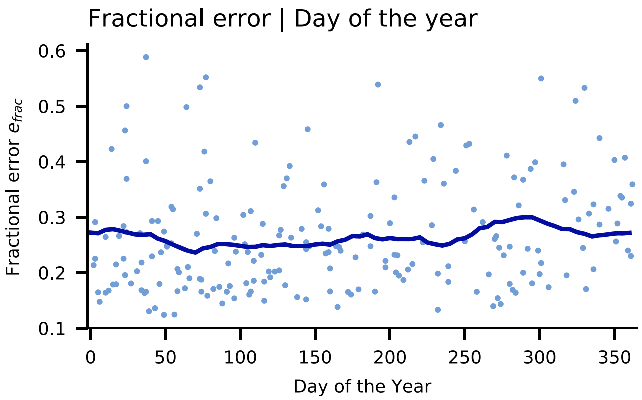

Figure A1. Fractional error of each observed wave event in the RIS as a function of day of the year (blue dots). The 31-day running mean is shown as blue line.

Acknowledgments
M. C. H. and P. D. B. were supported by NSFPLR 1246151, NSF OPP 1744856, and CAL DPR C1670002. B. D. C. gratefully acknowledges support from ONR Grants N000141512285 and N000141512598. S. T. G. was supported by the National Science Foundation (NSF) Grants OCE-1658001 and PLR-1425989, and by NASA Awards NNX14A078G and 80NSSC19K0059. A. J. M. was supported by NSF Grant OCE-1419306. This study forms a portion of the Ph.D. dissertation of M. C. H. We thank Guilherme Castelão for advice on data processing. This study could not have been possible without the scientific insight and field work of the Ross Ice Shelf team that includes P. Gerstoft, R. A. Stephen, R. C. Aster, D. A. Wiens, and A. A. Nyblade, whose efforts were instrumental in obtaining the seismic measurements used in this study. Seismic instruments and on-ice support were provided by the Incorporated Research Institutions for Seismology (IRIS) through the PASSCAL Instrument Center at New Mexico Tech. The RIS seismic data are archived at the IRIS Data Management Center (http://ds.iris.edu/ds/nodes/dmc/), with network code XH. Logistical support from the U.S. Antarctica Program and staff at McMurdo Station were critical and are much appreciated. The number of available wind observations were derived from CCMP Version-2.0 vector wind analyses, which are produced by Remote Sensing Systems. Data are available online (www.remss.com).

References

Abernathey, R. P., Cerovecki, I., Holland, P. R., Newsom, E., Mazloff, M., & Talley, L. D. (2016). Water-mass transformation by sea ice in the upper branch of the Southern Ocean overturning. *Nature Geoscience*, *9*, 596–601. https://doi.org/10.1038/ngeo2749

Adamson, D. S., Belcher, S. E., Hoskins, B. J., & Plant, R. S. (2006). Boundary-layer friction in midlatitude cyclones. *Quarterly Journal of the Royal Meteorological Society*, *132*, 101–124. https://doi.org/10.1256/qj.04.145

Ardhuin, F., Gille, S. T., Menemenlis, D., Rocha, C. B., Rascle, N., Chapron, B., et al. (2017). Small-scale open ocean currents have large effects on wind wave heights. *Journal of Geophysical Research: Oceans*, *122*, 4500–4517. https://doi.org/10.1002/2016JC012413

Ardhuin, F., Rogers, E., Babanin, A. V., Filipot, J.-F., Magne, R., Roland, A., et al. (2010). Semiempirical dissipation source functions for ocean waves. Part I: Definition, calibration, and validation. *Journal of Physical Oceanography*, *40*, 1917–1941. https://doi.org/10.1175/2010JPO4324.1

Ardhuin, F., Sutherland, P., Doble, M., & Wadhams, P. (2016). Ocean waves across the Arctic: Attenuation due to dissipation dominates over scattering for periods longer than 19 s. *Geophysical Research Letters*, *43*, 5775–5783. https://doi.org/10.1002/2016GL068204

Arrigo, K. R., van Dijken, G. L., & Strong, A. L. (2015). Environmental controls of marine productivity hot spots around Antarctica. *Journal of Geophysical Research: Oceans*, *120*, 5545–5565. https://doi.org/10.1002/2015JC010888

Atlas, R., Hoffman, R. N., Ardizzone, J., Leidner, S. M., Jusem, J. C., Smith, D. K., & Gombos, D. (2011). A cross-calibrated, multiplatform ocean surface wind velocity product for meteorological and oceanographic applications. *Bulletin of the American Meteorological Society*, *92*, 157–174. https://doi.org/10.1175/2010BAMS2946.1

Barber, N. F., & Ursell, F. (1948). The generation and propagation of ocean waves and swell. I. Wave periods and velocities. *Philosophical Transactions of the Royal Society A*, *240*, 527–560. https://doi.org/10.1098/rsta.1948.0005

Barnett, T. P. (1968). On the generation, dissipation, and prediction of ocean wind waves. *Journal of Geophysical Research*, *73*, 513–529. https://doi.org/10.1029/JB073i002p00513

Bates, H. F., & Shapiro, L. H. (1980). Long-period gravity waves in ice-covered sea. *Journal of Geophysical Research*, *85*, 1095–1100. https://doi.org/10.1029/JC085iC02p01095

Beare, R. J. (2007). Boundary layer mechanisms in extratropical cyclones. *Quarterly Journal of the Royal Meteorological Society*, *133*, 503–515. https://doi.org/10.1002/qj.30

Bengtsson, L., Hodges, K. I., & Keenlyside, N. (2009). Will extratropical storms intensify in a warmer climate? *Journal of Climate*, *22*, 2276–2301. https://doi.org/10.1175/2008JCLI2678.1

Bidlot, J.-R., Holmes, D. J., Wittmann, P. A., Lalbeharry, R., & Chen, H. S. (2002). Intercomparison of the performance of operational ocean wave forecasting systems with buoy data. *Weather and Forecasting*, *17*, 287–310. https://doi.org/10.1175/1520-0434(2002)017<0287:IOTPOO>2.0.CO;2

Blender, R., & Schubert, M. (2000). Cyclone tracking in different spatial and temporal resolutions. *Monthly Weather Review*, *128*, 377. https://doi.org/10.1175/1520-0493(2000)128<0377:CTIDSA>2.0.CO;2

Bourassa, M. A., Gille, S. T., Bitz, C., Carlson, D., Cerovecki, I., Clayson, C. A., et al. (2013). High-latitude ocean and sea ice surface fluxes: Challenges for climate research. *Bulletin of the American Meteorological Society*, *94*, 403–423. https://doi.org/10.1175/BAMS-D-11-00244.1

Brodzik, M. J., Billingsley, B., Haran, T., Raup, B., & Savoie, M. H. (2012). EASE-Grid 2.0: Incremental but significant improvements for Earth-gridded data sets. *ISPRS International Journal of Geo-Information*, *1*, 32–45. https://doi.org/10.3390/ijgi1010032

Brodzik, M., Billingsley, B., Haran, T., Raup, B., & Savoie, M. (2014). Correction: Brodzik, M . J., et al. EASE-Grid 2.0: Incremental but significant improvements for Earth-gridded data sets. ISPRS International Journal of Geo-Information 2012, 1, 32–45. *ISPRS International Journal of Geo-Information*, *3*, 1154–1156. https://doi.org/10.3390/ijgi3031154

Bromirski, P. D., Cayan, D. R., Helly, J., & Wittmann, P. (2013). Wave power variability and trends across the North Pacific. *Journal of Geophysical Research: Oceans*, *118*, 6329–6348. https://doi.org/10.1002/2013JC009189

Bromirski, P. D., Diez, A., Gerstoft, P., Stephen, R. A., Bolmer, T., Wiens, D. A., et al. (2015). Ross ice shelf vibrations. *Geophysical Research Letters*, *42*, 7589–7597. https://doi.org/10.1002/2015GL065284

Bromirski, P. D., & Duennebier, F. K. (2002). The near-coastal microseism spectrum: Spatial and temporal wave climate relationships. *Journal of Geophysical Research*, *107*, 2166. https://doi.org/10.1029/2001JB000265

Bromirski, P. D., Sergienko, O. V., & MacAyeal, D. R. (2010). Transoceanic infragravity waves impacting Antarctic ice shelves. *Geophysical Research Letters*, *37*, L02502. https://doi.org/10.1029/2009GL041488

Carranza, M. M., Gille, S. T., Franks, P. J. S., Johnson, K. S., Pinkel, R., & Girton, J. B. (2018). When mixed layers are not mixed. Storm-driven mixing and bio-optical vertical gradients in mixed layers of the Southern Ocean. *Journal of Geophysical Research: Oceans*, *123*, 7264–7289. https://doi.org/10.1029/2018JC014416

Cathles, L. M., Okal, E. A., & MacAyeal, D. R. (2009). Seismic observations of sea swell on the floating Ross Ice Shelf, Antarctica. *Journal of Geophysical Research*, *114*, F02015. https://doi.org/10.1029/2007JF000934

Cavaleri, L. (2009). Wave modeling—missing the peaks. *Journal of Physical Oceanography*, *39*, 2757–2778. https://doi.org/10.1175/2009JPO4067.1

Ceppi, P., Zappa, G., Shepherd, T. G., & Gregory, J. M. (2017). Fast and slow components of the extratropical atmospheric circulation response to CO_2 forcing. *Journal of Climate*, *31*, 1091–1105. https://doi.org/10.1175/JCLI-D-17-0323.1

Chawla, A., Spindler, D. M., & Tolman, H. L. (2013). Validation of a thirty year wave hindcast using the Climate Forecast System Reanalysis winds. *Ocean Modelling*, *70*, 189–206. https://doi.org/10.1016/j.ocemod.2012.07.005

Chen, Z., Bromirski, P. D., Gerstoft, P., Stephen, R. A., Lee, W. S., Yun, S., et al. (2019). Ross Ice Shelf icequakes associated with ocean gravity wave activity. *Geophysical Research Letters*, *46*, 8893–8902. https://doi.org/10.1029/2019GL084123

Collard, F., Ardhuin, F., & Chapron, B. (2009). Monitoring and analysis of ocean swell fields from space: New methods for routine observations. *Journal of Geophysical Research*, *114*, C07023. https://doi.org/10.1029/2008JC005215

Comiso, J. C., Kwok, R., Martin, S., & Gordon, A. L. (2011). Variability and trends in sea ice extent and ice production in the Ross Sea. *Journal of Geophysical Research*, *116*, C04021. https://doi.org/10.1029/2010JC006391

Copernicus Climate Change Service Climate Data Store (2017). Copernicus Climate Change Service (C3S) (2017): ERA5: Fifth generation of ECMWF atmospheric reanalyses of the global climate [accessed 02 03 2018]. Retrieved from https://cds.climate.copernicus.eu

Crawford, A. D., & Serreze, M. C. (2016). Does the summer Arctic frontal zone influence Arctic ocean cyclone activity? *Journal of Climate*, *29*, 4977–4993. https://doi.org/10.1175/JCLI-D-15-0755.1

Crawford, A. D., & Serreze, M. C. (2017). Projected changes in the Arctic frontal zone and summer Arctic cyclone activity in the CESM Large Ensemble. *Journal of Climate*, *30*, 9847–9869. https://doi.org/10.1175/JCLI-D-17-0296.1

Delpey, M. T., Ardhuin, F., Collard, F., & Chapron, B. (2010). Space-time structure of long ocean swell fields. *Journal of Geophysical Research*, *115*, C12037. https://doi.org/10.1029/2009JC005885

Doyle, J. D. (1995). Coupled ocean wave/atmosphere mesoscale model simulations of cyclogenesis. *Tellus A*, *47*, 766–778. https://doi.org/10.1034/j.1600-0870.1995.00119.x

Earl, D. J., & Deem, M. W. (2005). Parallel tempering: Theory, applications, and new perspectives. *Physical Chemistry Chemical Physics*, *7*, 3910–3916. https://doi.org/10.1039/B509983H

Erickson, Z. K., Thompson, A. F., Cassar, N., Sprintall, J., & Mazloff, M. R. (2016). An advective mechanism for deep chlorophyll maxima formation in southern Drake Passage. *Geophysical Research Letters*, *43*, 10,846–10,855. https://doi.org/10.1002/2016GL070565

Ferrari, R., & Wunsch, C. (2010). The distribution of eddy kinetic and potential energies in the global ocean. *Tellus A: Dynamic Meteorology and Oceanography*, *62*, 92–108. https://doi.org/10.1111/j.1600-0870.2009.00432.x

Foreman-Mackey, D., Hogg, D. W., Lang, D., & Goodman, J. (2013). Emcee: The MCMC Hammer. *Publications of the Astronomical Society of the Pacific*, *125*, 306–312. https://doi.org/10.1086/670067

Fox, C., & Squire, V. A. (1994). On the oblique reflexion and transmission of ocean waves at shore fast sea ice. *Philosophical Transactions of The Royal Society A Mathematical Physical and Engineering Sciences*, *347*, 185–218. https://doi.org/10.1098/rsta.1994.0044

Gallet, B., & Young, W. R. (2014). Refraction of swell by surface currents. *Journal of Marine Research*, *72*, 105–126. https://doi.org/10.1357/002224014813758959

Gelaro, R., McCarty, W., Suárez, M. J., Todling, R., Molod, A., Takacs, L., et al. (2017). The Modern-Era Retrospective Analysis for Research and Applications, Version 2 (MERRA-2). *Journal of Climate*, *30*, 5419–5454. https://doi.org/10.1175/JCLI-D-16-0758.1

Global Modeling and Assimilation Office (GMAO) (2015a). MERRA-2 const_2d_lnd_Nx: 2d, constants Land Surface Diagnostics V5.12.4, Greenbelt, MD, USA, Goddard Earth Sciences Data and Information Services Center (GES DISC), Accessed: [07/19/1018]. https://doi.org/10.5067/ME5QX6Q5IGGU

Global Modeling and Assimilation Office (GMAO) (2015b). MERRA-2 tavg1_2d_slv_Nx: 2d, 1-Hourly, Time-Averaged, Single-Level, Assimilation, Single-Level Diagnostics V5.12.4, Greenbelt, MD, USA, Goddard Earth Sciences Data and Information Services Center (GES DISC), Accessed: [07/19/1018]. https://doi.org/10.5067/VJAFPLI1CSIV

Goodman, J., & Weare, J. (2010). Ensemble samplers with affine invariance. *Communications in Applied Mathematics and Computational Sciences*, *5*, 65–80. https://doi.org/10.2140/camcos.2010.5.65

Gruber, N., Clement, D., Carter, B. R., Feely, R. A., van Heuven, S, Hoppema, M., et al. (2019). The oceanic sink for anthropogenic CO_2 from 1994 to 2007. *Science*, *363*, 1193–1199. https://doi.org/10.1126/science.aau5153

Hasselmann, K. (1963). A statistical analysis of the generation of microseisms. *Reviews of Geophysics*, *1*, 177–210. https://doi.org/10.1029/RG001i002p00177

Hasselmann, K., Barnett, T. P., Bouws, E., Carlson, H., Cartwright, D. E., Enke, K., et al. (1973). Measurements of wind-wave growth and swell decay during the Joint North Sea Wave Project (JONSWAP) (*Ergänzungsheft 8-12*).

Hasselmann, S., Hasselmann, K., Allender, J. H., & Barnett, T. P. (1985). Computations and parameterizations of the nonlinear energy transfer in a gravity-wave specturm. Part II: Parameterizations of the nonlinear energy transfer for application in wave models. *Journal of Physical Oceanography*, *15*, 1378–1391. https://doi.org/10.1175/1520-0485(1985)015<1378:CAPOTN>2.0.CO;2

Haumann, F. A., Gruber, N., Münnich, M., Frenger, I., & Kern, S. (2016). Sea-ice transport driving Southern Ocean salinity and its recent trends. *Nature*, *537*, 89–92. https://doi.org/10.1038/nature19101

Hell, M. C., Cornelle, B. D., Gille, S. T., Miller, A. J., & Bromirski, P. D. (2019). Identifying ocean swell generation events from Ross Ice Shelf seismic data. *Journal of Atmospheric and Oceanic Technology*, *36*, 2171–2189. https://doi.org/10.1175/JTECH-D-19-0093.1

Hodges, K. I., Hoskins, B. J., Boyle, J., & Thorncroft, C. (2003). A comparison of recent reanalysis datasets using objective feature tracking: Storm tracks and tropical easterly waves. *Monthly Weather Review*, *131*, 2012–2037. https://doi.org/10.1175/1520-0493(2003)131<2012:ACORRD>2.0.CO;2

Hodges, K. I., Lee, R. W., & Bengtsson, L. (2011). A comparison of extratropical cyclones in recent reanalyses ERA-Interim, NASA MERRA, NCEP CFSR, and JRA-25. *Journal of Climate*, *24*, 4888–4906. https://doi.org/10.1175/2011JCLI4097.1

Holland, P. R., & Kwok, R. (2012). Wind-driven trends in Antarctic sea-ice drift. *Nature Geoscience*, *5*, 872–875. https://doi.org/10.1038/ngeo1627

Hoskins, B. J., & Hodges, K. I. (2002). New perspectives on the Northern Hemisphere winter storm tracks. *Journal of the Atmospheric Sciences*, *59*, 1041–1061.

Hoskins, B. J., & Hodges, K. I. (2005). A new perspective on Southern Hemisphere storm tracks. *Journal of Climate*, *18*, 4108–4129. https://doi.org/10.1175/JCLI3570.1

Johnson, G. C., & Bryden, H. L. (1989). On the size of the Antarctic Circumpolar Current. *Deep Sea Research Part A. Oceanographic Research Papers*, *36*, 39–53. https://doi.org/10.1016/0198-0149(89)90017-4

Kidston, J., Taschetto, A. S., Thompson, D. W. J., & England, M. H. (2011). The influence of Southern Hemisphere sea-ice extent on the latitude of the mid-latitude jet stream. *Geophysical Research Letters*, *38*, L15804. https://doi.org/10.1029/2011GL048056

Kirkpatrick, S., Gelatt, C. D., & Vecchi, M. P. (1983). Optimization by simulated annealing. *Science*, *220*, 671–680. https://doi.org/10.1126/science.220.4598.671

Kudryavtsev, V., Golubkin, P., & Chapron, B. (2015). A simplified wave enhancement criterion for moving extreme events. *Journal of Geophysical Research: Oceans*, *120*, 7538–7558. https://doi.org/10.1002/2015JC011284

Kwok, R. (2005). Ross Sea ice motion, area flux, and deformation. *Journal of Climate*, *18*, 3759–3776. https://doi.org/10.1175/JCLI3507.1

Li, M., Liu, J., Wang, Z., Wang, H., Zhang, Z., Zhang, L., & Yang, Q. (2013). Assessment of sea surface wind from NWP reanalyses and satellites in the Southern Ocean. *Journal of Atmospheric and Oceanic Technology*, *30*, 1842–1853. https://doi.org/10.1175/JTECH-D-12-00240.1

Li, Q., Webb, A., Fox-Kemper, B., Craig, A., Danabasoglu, G., Large, W. G., & Vertenstein, M. (2016). Langmuir mixing effects on global climate: WAVEWATCH III in CESM. *Ocean Model.*, *103*, 145–160. https://doi.org/10.1016/j.ocemod.2015.07.020

Lu, J., Chen, G., & Frierson, D. M. W. (2010). The position of the midlatitude storm track and eddy-driven westerlies in aquaplanet AGCMs. *Journal of the Atmospheric Sciences*, *67*, 3984–4000. https://doi.org/10.1175/2010JAS3477.1

MacAyeal, D. R., Okal, E. A., Aster, R. C., & Bassis, J. N. (2009). Seismic observations of glaciogenic ocean waves (micro-tsunamis) on icebergs and ice shelves. *Journal of Glaciology*, *55*, 193–206. https://doi.org/10.3189/002214309788608679

Massom, R. A., Scambos, T. A., Bennetts, L. G., Reid, P., Squire, V. A., & Stammerjohn, S. E. (2018). Antarctic ice shelf disintegration triggered by sea ice loss and ocean swell. *Nature*, *558*, 383–389. https://doi.org/10.1038/s41586-018-0212-1

Meissner, T., & Wentz, F. J. (2009). Wind-vector retrievals under rain with passive satellite microwave radiometers. *IEEE Transactions on Geoscience and Remote Sensing*, *47*, 3065–3083. https://doi.org/10.1109/TGRS.2009.2027012

Miles, J. W. (1960). On the generation of surface waves by turbulent shear flows. *Journal of Fluid Mechanics*, *7*, 469–478. https://doi.org/10.1017/S0022112060000220

Munk, W. H. (1947). Tracking storms by forerunners of swell. *J. Meteor.*, *4*, 45–57. https://doi.org/10.1016/0146-6313(56)90061-2

Munk, W. H., Miller, G. R., Snodgrass, F. E., & Barber, N. F. (1963). Directional recording of swell from distant storms. *Philosophical Transactions of the Royal Society A*, *255*, 505–584. https://doi.org/10.1098/rsta.1963.0011

Munk, W. H., & Palmén, E. (1951). Note on the dynamics of the Antarctic Circumpolar Current1. *Tellus*, *3*, 53–55. https://doi.org/10.1111/j.2153-3490.1951.tb00776.x

Munk, W. H., & Snodgrass, F. E. (1957). Measurements of southern swell at Guadalupe Island. *Deep Sea Research (1953)*, *4*, 272–286. https://doi.org/10.1016/0146-6313(56)90061-2

Neiman, P. J., & Shapiro, M. A. (1993). The life cycle of an extratropical marine cyclone. Part I: Frontal-cyclone evolution and thermodynamic air-sea interaction. *Monthly Weather Review*, *121*, 2153–2176. https://doi.org/10.1175/1520-0493(1993)121<2153:TLCOAE>2.0.CO;2

Neiman, P. J., Shapiro, M. A., & Fedor, L. S. (1993). The life cycle of an extratropical marine cyclone. Part II: Mesoscale structure and diagnostics. *Monthly Weather Review*, *121*, 2177–2199. https://doi.org/10.1175/1520-0493(1993)121<2177:TLCOAE>2.0.CO;2

Neu, U., Akperov, M. G., Bellenbaum, N., Benestad, R., Blender, R., Caballero, R., et al. (2012). IMILAST: A community effort to intercompare extratropical cyclone detection and tracking algorithms. *Bulletin of the American Meteorological Society*, *94*, 529–547. https://doi.org/10.1175/BAMS-D-11-00154.1

Newville, M., Stensitzki, T., Allen, D. B., & Ingargiola, A. (2014). *LMFIT: Non-linear least-square minimization and curve-fitting for Python*. Zenodo. https://doi.org/10.5281/zenodo.11813

Ogle, S. E., Tamsitt, V., Josey, S. A., Gille, S. T., Cerovečki, I., Talley, L. D., & Weller, R. A. (2018). Episodic Southern Ocean heat loss and its mixed layer impacts revealed by the farthest south multiyear surface flux mooring. *Geophysical Research Letters*, *45*, 5002–5010. https://doi.org/10.1029/2017GL076909

Phillips, O. M. (1985). Spectral and statistical properties of the equilibrium range in wind-generated gravity waves. *Journal of Fluid Mechanics*, *156*, 505–531. https://doi.org/10.1017/S0022112085002221

Pierson, W. J., & Moskowitz, L. (1964). A proposed spectral form for fully developed wind seas based on the similarity theory of S. A. Kitaigorodskii. *Journal of Geophysical Research*, *69*, 5181–5190. https://doi.org/10.1029/JZ069i024p05181

Rascle, N., Ardhuin, F., Queffeulou, P., & Croizé-Fillon, D. (2008). A global wave parameter database for geophysical applications. Part 1: Wave-current–turbulence interaction parameters for the open ocean based on traditional parameterizations. *Ocean Modelling*, *25*, 154–171. https://doi.org/10.1016/j.ocemod.2008.07.006

Ren, D., & Leslie, L. M. (2014). Effects of waves on tabular ice-shelf calving. *Earth Interact.*, *18*, 1–28. https://doi.org/10.1175/EI-D-14-0005.1

Rocha, C. B., Chereskin, T. K., Gille, S. T., & Menemenlis, D. (2015). Mesoscale to submesoscale wavenumber spectra in Drake Passage. *Journal of Physical Oceanography*, *46*, 601–620. https://doi.org/10.1175/JPO-D-15-0087.1

Shepherd, A., Ivins, E. R., A, Geruo, Barletta, V. R., Bentley, M. J., Bettadpur, S., et al. (2012). A reconciled estimate of ice-sheet mass balance. *Science*, *338*, 1183–1189. https://doi.org/10.1126/science.1228102

Simmonds, I., & Keay, K. (2000). Mean Southern Hemisphere extratropical cyclone behavior in the 40-Year NCEP–NCAR Reanalysis. *Journal of Climate*, *13*(5), 873–885.

Simmonds, I., Keay, K., & Lim, E.-P. (2003). Synoptic activity in the seas around Antarctica. *Monthly Weather Review*, *131*, 272–288. https://doi.org/10.1175/1520-0493(2003)131<0272:SAITSA>2.0.CO;2

Simmonds, I., & Murray, R. J. (1999). Southern extratropical cyclone behavior in ECMWF analyses during the FROST special observing periods. *Weather Forecasting*, *14*, 878–891. https://doi.org/10.1175/1520-0434(1999)014<0878:SECBIE>2.0.CO;2

Simmonds, I., & Rudeva, I. (2014). A comparison of tracking methods for extreme cyclones in the Arctic basin. *Tellus A*, *66*. https://doi.org/10.3402/tellusa.v66.25252

Smith, S. D. (1988). Coefficients for sea surface wind stress, heat flux, and wind profiles as a function of wind speed and temperature. *Journal of Geophysical Research: Oceans*, *93*, 15,467–15,472. https://doi.org/10.1029/JC093iC12p15467

Snodgrass, F. E., Groves, G. W., Hasselmann, K. F., Miller, G. R., Munk, W. H., & Powers, W. H. (1966). Propagation of ocean swell across the Pacific. *Philosophical Transactions of The Royal Society A*, *259*, 431–497. https://doi.org/10.1098/rsta.1966.0022

Squire, V. A. (2007). Of ocean waves and sea-ice revisited. *Cold Regions Science and Technology*, *49*, 110–133. https://doi.org/10.1016/j.coldregions.2007.04.007

Squire, V. A., & Allan, A. J. (1980). Propagation of flexural gravity waves in sea ice. In R. S. Pritchard (Ed.), *Sea ice processes and models* (pp. 327–338). Seattle: University of Washington Press.

Stopa, J. E., Sutherland, P., & Ardhuin, F. (2018). Strong and highly variable push of ocean waves on Southern Ocean sea ice. *PNAS*, *115*, 5861–5865. https://doi.org/10.1073/pnas.1802011115

Tolman, H. L. (2009). User manual and system documentation of WAVEWATCH III TM version 3.14. *Tech. Note MMAB Contrib.*, *276*, 220.

Toudal Pedersen, L., Dybkjær, G., Eastwood, S., Heygster, G., Ivanova, N., Kern, S., et al. (2017). *ESA sea ice climate change initiative (Sea_Ice_cci): Sea Ice Concentration Climate Data Record from the AMSR-E and AMSR-2 instruments at 50km grid spacing, version 2.1*: Centre for Environmental Data Analysis (CEDA). https://doi.org/10.5285/5f75fcb0c58740d99b07953797bc041e

Trenberth, K. E. (1991). Storm tracks in the Southern Hemisphere. *Journal of the Atmospheric Sciences*, *48*, 2159–2178.

Vaughan, G. L., Bennetts, L. G., & Squire, V. A. (2009). The decay of flexural-gravity waves in long sea ice transects. *Proceedings of the Royal Society of London Mathematical Physical and Engineering Sciences*, *465*, 2785–2812. https://doi.org/10.1098/rspa.2009.0187

Villas Bôas, A. B., Gille, S. T., Mazloff, M. R., & Cornuelle, B. D. (2017). Characterization of the deep water surface wave variability in the California Current Region. *Journal of Geophysical Research: Oceans*, *122*, 8753–8769. https://doi.org/10.1002/2017JC013280

Wadhams, P., & Doble, M. J. (2009). Sea ice thickness measurement using episodic infragravity waves from distant storms. *Cold Regions Science and Technology*, *56*, 98–101. https://doi.org/10.1016/j.coldregions.2008.12.002

Wang, X. L., Feng, Y., Chan, R., & Isaac, V. (2016). Inter-comparison of extra-tropical cyclone activity in nine reanalysis datasets. *Atmospheric Research*, *181*, 133–153. https://doi.org/10.1016/j.atmosres.2016.06.010

Wentz, F. J., J. Scott, R., Hoffman, M., Leidner, R., & Atlas, J. A. (2015). Remote Sensing Systems Cross-Calibrated Multi-Platform (CCMP) 6-hourly ocean vector wind analysis product on 0.25 deg grid, Version 2.0., 2014 to 2016. Remote Sensing Systems, Santa Rosa, CA, Available online at www.remss.com/measurements/ccmp. [Accessed 05 06 2018].

Wernli, H., & Schwierz, C. (2006). Surface cyclones in the ERA-40 dataset (1958–2001). Part I: Novel identification method and global climatology. *Journal of the Atmospheric Sciences*, *63*, 2486–2507. https://doi.org/10.1175/JAS3766.1

Wiens, D., Bromirski, P., Aster, R., Stephen, R., & Gerstoft, P. (2014). Collaborative research: Dynamic response of the Ross Ice Shelf to wave-induced vibrations and collaborative research: Mantle structure and dynamics of the ross sea from a passive seismic deployment on the Ross Ice Shelf. International Federation of Digital Seismograph Network, https://doi.org/10.7914/SN/XH2014

Williams, G., Maksym, T., Wilkinson, J., Kunz, C., Murphy, C., Kimball, P., & Singh, H. (2015). Thick and deformed Antarctic sea ice mapped with autonomous underwater vehicles. *Nature Geoscience*, *8*, 61–67. https://doi.org/10.1038/ngeo2299